



TITLE:

Wind Resistance Evaluation of Existing Standing Buddha Statue Using 3D Laser Scanning and CFD

AUTHOR(S):

Hnin, Thinzar; Noguchi, Kyohei; Yagi, Tomomi

CITATION:

Hnin, Thinzar ...[et al]. Wind Resistance Evaluation of Existing Standing Buddha Statue Using 3D Laser Scanning and CFD. Journal of Structural Engineering 2023, 149(8): 04023095.

ISSUE DATE:

2023-08

URL:

<http://hdl.handle.net/2433/283986>

RIGHT:

This material may be downloaded for personal use only. Any other use requires prior permission of the American Society of Civil Engineers. This material may be found at <https://doi.org/10.1061/jsendh.steng-11709>.; This is not the published version. Please cite only the published version. この論文は出版社版ではありません。引用の際には出版社版をご確認ください。

1 Wind Resistance Evaluation of Existing Standing Buddha Statue Using 3D Laser Scanning and CFD

2 ABSTRACT

3 Underestimating the aerodynamic forces acting on structures can lead to them sustaining severe damage.
4 Currently, there are limited studies on the wind flow around complex-shaped tall structures such as the Buddha
5 statue and the aerodynamic forces acting on them. This study discusses the applicability of 3D terrestrial laser
6 scanning in the 3D modeling of an existing complex-shaped standing Buddha statue. This study also aims to
7 shed light on the wind resistance evaluation for the maintenance of a contemporary standing Buddha statue.
8 Large Eddy Simulation (LES) was utilized to calculate the wind flow around it. The results showed that there
9 was no recirculation region at its top. The horseshoe vortex moved closer to the Buddha statue as the angle of
10 attack (AOA) increased. However, the size of the wake region decreased. Sudden changes in the aerodynamic
11 force coefficients and Strouhal number were observed in the Buddha statue—owing to vortices caused by the
12 cross-sectional variations in shape and a setback. Finally, the most vulnerable parts of the Buddha statue which
13 might require optimal maintenance and renovation are mentioned. Results from this study can be used in
14 developing maintenance techniques for similar complex-shaped structures.

15 Keywords: Complex-shaped tall structure, standing Buddha statue, 3D terrestrial laser scanning, wind resistance
16 evaluation, flow field characteristics, maintenance and renovation

17 INTRODUCTION

18
19 Increasing inbound and outbound tourism usually creates various types of jobs, increases the gross
20 domestic product (GDP), and promotes cross-cultural communication. Thus, many countries strive to possess
21 distinct natural and artificial landmarks. Generally, natural landmarks include geological characteristic features,
22 such as mountains or plateaus, while artificial landmarks include innovative and distinctive buildings.
23 Accordingly, churches with spires; minarets—usually near mosques; and Buddha statues with different mudras,
24 which are often very tall and noticeable even from far distances; have been built to serve as landmarks. According
25 to historical records, structures that are improperly maintained can sustain severe damage and result in serious

26 human casualties. To avoid this, high-rise structures require regular proper maintenance. However, there are still
27 limitations as most available building codes only provide information on basic shapes such as rectangular and
28 circular cylinders and recommend wind-tunnel testing or numerical simulations for complex-shaped structures
29 instead. If wind tunnel testing is infeasible owing to technical unavailability, financial restrictions, and existing
30 structural conditions, which is especially common in developing countries, computational fluid dynamics (CFD)
31 simulation can be used to fill this gap.

32 Generally, the structural specifications and external configurations of the structure are required to
33 perform CFD simulations. This type of information can be obtained from architectural drawings, detailed
34 structural drawings, computer-aided design (CAD) files, and structural analysis models. However, such sources
35 may be unavailable for historical monuments or existing structures with unknown or unverified construction
36 details. Therefore, alternative advanced technologies, such as the geographic information system (GIS); light
37 detection and ranging (LIDAR); airborne laser scanning (ALS), drone 3D modeling; and 3D terrestrial laser
38 scanning, are widely utilized. Among them, the 3D terrestrial laser scanning method has become quite popular
39 for obtaining the detailed structural configurations of existing structures. Hess et al. (2018) also used this method
40 to acquire data for the structural health assessment, visualization, and analysis of the Baptistery of St John in
41 Florence, Italy. However, the applicability of 3D terrestrial laser scanning for existing tall and complex-shaped
42 structures is still unclear and further research is required. In the CFD simulation, the accuracy of the simulation
43 is affected by the handling of the complex geometry and grid resolution of the structure by the mesh generation
44 method. Mavriplis (2007, 2008) discussed that the unstructured mesh performed better than the structured
45 meshes in parallel computations. However, using an unstructured mesh may not always be the best approach for
46 addressing complex geometrics and/or adaptive meshing requirements. When the wind load acting on a standard
47 tall building was calculated, the Large Eddy Simulation (LES) results agreed well with the experimental results
48 in the along-wind and across-wind load calculations, while the torsional wind load showed some discrepancies.
49 Therefore, Dagnew and Bitsuamlak (2013) summarized that overall, LES seemed suitable for wind load
50 evaluation. Phuc et al. (2018) also mentioned that the Smagorinsky model agreed well with the wind tunnel
51 experimental results for isolated rectangular high-rise buildings under uniform flow.

52 Irwin et al. (2008), and Irwin (2010) stated that the structures buffeted by the wind experienced push
 53 and pull in the direction perpendicular to the wind flow, and a vortex formed on the side of the structures. When
 54 these vortices are alternatively organized in patterns and rock the building from each side, the resulting impact
 55 can be severe. This impact can be reduced by modifying the aerodynamic design of tall buildings using various
 56 shaping strategies. Baker et al. (2007) stated that even for the highest tower in the world, the Burj Khalifa (Burj
 57 Dubai), a “Y” shaped plan was implemented to reduce the aerodynamic forces acting on the tower. Additionally,
 58 the setbacks of the Burj Dubai building were designed to change the building width according to the height so
 59 that the vortices could not harm the building.

60 Figure 1 shows the mean flow topology around the basic finite circular cylinder, separated into three
 61 areas: the horseshoe vortex, separated flow over the free end, and the wake region. A horseshoe vortex is formed
 62 on the ground when the upstream flow separates owing to an adverse pressure gradient. This vortex can cause
 63 material elimination at the cylinder-wall junction, which can lead to failure of the pier, bridge, and pylon. An
 64 arch vortex is formed in the rear recirculation region, known as the wake region. This vortex and the trailing
 65 vortices, which are located downstream of the reattachment, enhance the complexity of the flow structures and
 66 create a strong turbulent flow around the finite circular cylinder (Pattenden et al. 2005).

67 In this study, the 3D terrestrial laser scanning (TLS) method was used to capture the external
 68 configuration of a complex-shaped tall Buddha statue, and the scanned data were used to construct the 3D
 69 configuration of the statue. Hence, the present study filled an existing gap in the applicability of 3D terrestrial
 70 laser scanning on the existing complex-shaped structure. LES, the Smagorinsky model (Smagorinsky, 1963),
 71 and unstructured mesh methods were used to investigate the wind flow around the Buddha statue. The paper is
 72 organized according to the following sections. First, the paper presents basic information regarding the target
 73 Buddha statue, 3D laser scanning, and LES. Then, it describes the characteristics of the 3D flow field around the
 74 Buddha statue, and it discusses the aerodynamic force coefficients, vortex shedding frequency, and Strouhal
 75 number of the Buddha statue. Finally, the paper mentions the parts of the Buddha statue that require careful
 76 treatment during maintenance and renovation. This paper also summarizes the flow characteristics around
 77 different parts of the Buddha statue and highlights the most vulnerable parts of it which should be noted for
 78 disaster prevention of similar structures in real practice.

79 LAYKYUN SEKKYA STANDING BUDDHA STATUE

80

81 The “Laykyun Sekkya Standing Buddha Statue,” also known as the “Maha Bodhi Ta Htaung Standing
82 Buddha,” is the sculpture of the Gautama Buddha that is used as a model in this study. It is a hollow-type Buddha
83 statue. It is located on the Po Khaung Mountain, Monywa City, Sagaing Region, Myanmar. The overall height
84 of the statue is approximately 129 m with the lotus throne and 116 m without it. The statue was constructed
85 between 1996 and 2008 with the aim of becoming an attraction site in the Sagaing region. For constructing the
86 statue, reinforced concrete was used from the foundation to the 10th story, steel was used from the 11th story to
87 the neck, and fiberglass was used for the head. As shown in Figure 2, the Laykyun Sekkya Standing Buddha
88 Statue is recorded as the third tallest statue in the world, as of 2022. The case study area, Monywa, has a hot
89 semi-arid climate with extremely hot early monsoon months. Tropical cyclone tracks in the Bay of Bengal have
90 indicated that tropical cyclones originated mostly from the southwest of Monywa, during 1983–2012 (Hirano,
91 2021). From 2000 to 2010, three tropical cyclones affected this area with maximum sustained wind speeds of
92 35, 50, and 135 km h⁻¹ (UNDP, 2011). Consequently, there is growing concern among residents about the safety
93 of the Buddha statue.

94 THREE-DIMENSIONAL SCANNING AND MODELING

95

96 Recent developments in remote sensing and data acquisition technology have made structural health
97 monitoring and assessment more flexible and time-efficient. However, there are still some limits and boundaries
98 in applying these technologies in existing complex-shaped tall structures. Therefore, this study intends to
99 introduce the 3D modeling procedure of a structure, in which the design information is unavailable, and shape
100 is complicated to manually reproduce. In this study, the 3D terrestrial laser scanning method was used to collect
101 data on the geometry of the Buddha statue as the availability of the CAD data and structural design information
102 is limited to this structure. This method also requires only a few input parameters and can provide accurate
103 measurement within a short period. The collected scan data were mainly pre-processed and inputted into the 3D
104 model using FARO SCENE software (FARO Technologies, Inc., USA).

105 **Terrestrial Laser Scanning (TLS)**

106 A mid-range ground-based terrestrial-type phase-shift laser scanner, Faro Focus 3D X 330, was used to
 107 obtain the exterior configuration of the Buddha statue. The scanner collects information such as the size, shape,
 108 and texture of the object using a movable infrared laser light line. In addition, it also takes images with an
 109 onboard camera to color the point cloud. Hence, it is necessary to prevent moving obstacles such as humans and
 110 animals from interfering during 3D laser scanning as this hinders scan recognition and the registration of global
 111 coordinates. The polar coordinates of the distance, vertical angle, and horizontal angle are obtained from the
 112 mirror and horizontal rotations of the scanner and these coordinates are transformed into Cartesian coordinates.
 113 The targeted structure is recorded as a “point cloud,” which contains a set of points with each point containing
 114 coordinates of the location of the structure in space.

115 To obtain the optimal view of the Buddha statue with its overall height, minimal obstruction, and
 116 sufficient overlap, 36 locations were used, as illustrated in Figure 3 (a). The scanner captured detailed
 117 information on the lotus throne and the lower parts of the Buddha statue from 11 blue points, the middle parts
 118 of the Buddha statue from 14 violet points, and the head, shoulder, and remaining top parts of the Buddha statue
 119 from 11 yellow points. One random draft scan is illustrated in Figure 3 (b). The overlap between each scan
 120 location was maintained at 60% because the targetless scanning method was applied. The scans from the two
 121 red points were not used in the visualization process because of obstructions. The distance from the Buddha
 122 statue to the furthest scanner location was 303.74 m and the maximum probable error for a single point within
 123 this distance was 24.3 mm. The equipment settings and scanning duration at one location were within
 124 approximately 30 min for ½ resolution and 3× quality color scans. The resolution determines the density of data
 125 points and the distance between those points. The “½ resolution” is equivalent to approximately 3.068 mm point
 126 spacing at a 10 m distance. Scan quality determines the noise in the measurement based on the incoming signal
 127 strength by increasing the observation time. The quality factor 3× has an observation time of approximately 6
 128 μs per scan point. Built-in sensors such as global positioning system (GPS), compass, inclinometer, and altimeter
 129 were used together with far distance optimization setting to modify the point cloud during scan registration. The
 130 far distance optimization setting considers the distance between the scanner and statue to be larger than 20 m
 131 and only focuses on the measurement accuracy of objects located in the far distances.

132 **3D Modelling**

133 The coordinate data were sorted, and point clouds were also extracted from all the 34 panorama 360°
 134 draft scans of the Buddha statue. First, the initial alignment was performed by manually identifying the mutual
 135 parts of each scan. Then, the Buddha statue was simply divided into four clusters with customized automatic
 136 scan-to-scan alignment. After all the clusters were roughly aligned, the common reference planes and points
 137 were used to position these clusters into one global coordinate system, as illustrated in Figure 4. The total
 138 alignment error for the 3D modeling of the Buddha statue was 23.4 mm. The average point spacing of the 3D
 139 statue model was approximately 0.1 m.

140 During the generation of the project point cloud dataset, there were limitations in extracting data from
 141 the draft scans for black surfaces of the Buddha Statue, such as the hair and glasses parts. Generally, a black
 142 surface has a slight or no reflectivity. The poor reflectivity of the black surface and the sky-high height of the
 143 Buddha statue made it difficult for the 3D laser scanner to capture data from these areas. Therefore, the hair part
 144 of the Buddha statue was manually reproduced using FreeCAD software due to its low point density. The height
 145 (H), width (B), and side length (L) of the Buddha statue at the base were 129, 47.63, and 43.47 m, respectively.
 146 Since the exterior configuration of the statue was complex, the surface mesh of the 3D model generated from
 147 the scans contained twists and overlaps. These meshes were cleaned and repaired into approximately 22 mm
 148 meshes using Autodesk Meshmixer. The final 3D replica model of the Laykyun Sekkya Standing Buddha statue
 149 is shown in Figure 5. In this study, the total alignment error of the Buddha statue (23.4 mm) was only about
 150 0.02–0.05 % compared to the statue’s overall dimension, which was unlikely to change the simulation results in
 151 a significant way.

152 **COMPUTATIONAL FLUID DYNAMICS SIMULATION**

153
 154 The unsteady flow field around the standing Buddha statue and its aerodynamic characteristics resulting
 155 from its complex shape were calculated by performing LES using OpenFOAM 4.0. The governing equations
 156 used were the filtered incompressible Navier–Stokes equations and the equation of continuity:

$$157 \quad \frac{\partial \bar{u}_i}{\partial x_i} = 0 \quad (1)$$

158
$$\frac{\partial \bar{u}_i}{\partial t} + \bar{u}_j \frac{\partial \bar{u}_i}{\partial x_j} = - \frac{1}{\rho} \frac{\partial \bar{p}}{\partial x_i} + \frac{\partial}{\partial x_j} \left\{ (v + v_{SGS}) \left(\frac{\partial \bar{u}_i}{\partial x_j} + \frac{\partial \bar{u}_j}{\partial x_i} \right) \right\} \quad (2)$$

159 where \bar{u}_i is the filtered velocity, v is the viscosity, \bar{p} is the filtered pressure, ρ is the density, and v_{SGS} is the
160 subgrid-scale eddy viscosity coefficient, which was modeled based on the Smagorinsky model which is
161 represented as follows:

162
$$v_{SGS} = (C_s f_s \Delta)^2 |\bar{D}| \quad (3)$$

163 where \bar{D} is the strain rate tensor, Δ is the filter width, f_s is the damping function that corrects the value of v_{SGS}
164 near the wall, and C_s is the Smagorinsky constant, which was set as 0.12.

165 **Computational Domain**

166 Considering that tropical cyclones come mostly from the southwest and that the Buddha statue was
167 designed considering ones that came from the west, four different wind directions were considered during the
168 simulation. These wind directions were noted as the along-wind direction ($\alpha = 0^\circ$), west ($\alpha = 5^\circ$), southwest (α
169 $= 50^\circ$), and across-wind ($\alpha = 90^\circ$). LES was performed for a finite circular cylinder with the diameter of an
170 average statue's width ($B_{avg} = 30.22$ m) and height ($H = 129$ m) to validate the numerical simulations of the
171 Buddha statue. For all the simulation cases, the x-axis was the along-wind direction, and the y-axis was the
172 across-wind direction. The dimensions of the computational domains were determined according to standards
173 specified by the Architectural Institute of Japan (AIJ, 2017). The total computational domain size was $24.5 B$ (x)
174 $\times 21 B$ (y) $\times 2 H$ (z), as illustrated in Figure 6 (a). The blockage ratio in the across-wind direction was between
175 1.57 and 2.5%. Ten probes were embedded inside the computational domain for the interpretation of the flow
176 around the models as shown in Figure 6 (b) and the velocities in the wake region were also recorded. In this
177 study, both the Buddha statue and circular cylinder models were rigid. Both were equally divided into
178 approximately 26 parts ($0.039 D$ each) for a detailed representation of the aerodynamic characteristics of the
179 complex configuration. The topographic effects are neglected in this calculation to study the flow patterns and
180 aerodynamic characteristics produced solely by the Buddha statue.

181 **Surface Mesh and Volume Mesh**

182 Since unstructured-mesh methods were proven to be more convenient and successful in handling
183 complex geometries, one such method, anisotropic tetrahedral mesh generation, was applied to reproduce the
184 complex shape of the Buddha statue using Pointwise (VINAS, Japan), a mesh generation software. As the
185 windows around the Buddha statue did not contribute to the flow separation, they were considered not to affect
186 the simulation and simplified them as a plain surface to reduce the mesh number. Triangle and quad mesh cells
187 were used to generate the surface meshes of the statue. The average spacing between each grid (Δs) was around
188 0.25 m, which was $B/190$ (B is the width of the Buddha statue). The meshing is well reflected in the low point
189 density near the top of the statue. The volume mesh was mainly composed of tetrahedral, pyramidal, prism, and
190 hexahedral cells. This allowed us to efficiently reproduce the complex shapes of the Buddha statue and reduce
191 the total grid number. The height of the first cell near the Buddha statue was 0.09 m ($B/530$) and that of the last
192 cell was 10 m ($B/5$). The total grid number of each simulation case was approximately between 8.8×10^6 and
193 10.2×10^6 for different angle of attack (AOA) cases. The meshes near the Buddha statue and the circular cylinder
194 is shown in Figure 6 (c) and (d), respectively.

195 **Boundary Conditions**

196 The logarithmic inlet wind profile was calculated according to Equations (4) and (5), where U is the
197 wind velocity, U^* is the friction velocity, κ is the von Kármán's constant, with a value of 0.41, z is the vertical
198 coordinate, z_0 is the surface roughness height of 0.01 m for exposure category C, z_g is the minimum z-coordinate
199 (in m), and U_{ref} is the reference wind velocity of 31.3 m s^{-1} at 10 m above the ground surface, as specified by the
200 Myanmar National Building Code (MNBC).

201
$$U = \frac{U^*}{\kappa} \ln \left(\frac{z - z_g + z_0}{z_0} \right) \quad (4)$$

202
$$U^* = \kappa \frac{U_{ref}}{\ln \left(\frac{z_{ref} + z_0}{z_0} \right)} \quad (5)$$

203 At the outlet boundary, the gradient of the velocity in the streamwise direction and pressure was zero.
204 For the ground surface, an atmospheric boundary layer with a roughness length of 0.01 m for open terrains,

205 belonging to Exposure C, was used as it provided a better turbulence kinematic viscosity for atmospheric velocity
206 profiles. On the model surface, the wall function described in Equation (6), proposed by Spalding (1960), was
207 utilized. For the other surfaces, a slip boundary condition was applied.

$$208 \quad y^+ = u^+ + \frac{1}{E} \left[e^{\kappa u^+} - 1 - \kappa u^+ - \frac{1}{2}(\kappa u^+)^2 - \frac{1}{6}(\kappa u^+)^3 \right] \quad (6)$$

209 Numerical Algorithms

210 The first-order implicit Euler method was used for time advancement, and the second-order least squares
211 discretization scheme was followed to compute the gradient terms. All the divergence schemes were calculated
212 based on a second-order linear upwind scheme. For pressure-velocity coupling, the pressure-implicit with
213 splitting of operators (PISO) algorithm was used (Irwin, 2010).

214 The Reynolds number is defined as $Re = U_H B / \nu$, where U_H is the wind velocity at the height of the
215 model (m/s), B is the width of the model in the along-wind direction (m), and ν is the kinematic viscosity (m^2
216 s^{-1}). The mean wind velocity at the height of the Buddha statue (U_H) was around 42.88 m s^{-1} , resulting in the
217 statue and circular cylinder having Reynolds numbers of 1.30×10^4 and 2.04×10^4 , respectively. The non-
218 dimensional average time is defined as $t^* = U_H t / B$, where t is the physical simulation time. In this study, the
219 simulations were carried out for about $200 t^*$ to ensure statistical convergence and full flow field development.
220 For further calculation and sampling of the aerostatic force coefficients, an average duration of about $150 t^*$ after
221 a preliminary calculation of about $50 t^*$ was used. The time step (Δt) was 5.0×10^{-4} and the maximum Courant
222 number was around 1.5. This guaranteed a stable simulation for an implicit scheme on the unstructured grid. The
223 sampling time was 10 ms (100 Hz), and the sampling number was 20,000.

224 In this section, the visualization of the flow field around the models is presented in terms of time-
225 averaged normalized velocity magnitude and streamlines (Smits and Lim, 2000). The length of the recirculation
226 region (L_r) is defined as the distance between the centre of the model and the near-wake saddle point in the time-
227 averaged flow field Yoon et al. (2010). The width of the wake region (d') is defined as the lateral distance at a
228 given streamwise location between two points situated on opposite sides of the model centerline, distinguishing

229 the outer flow from the rotational wake flow (Roshko, 1954). The distance between the centres of the vortices
 230 in each pair was measured as the distance between each vortex pair (d_{pair}).

231 Mean Velocity Profiles

232 The mean along-wind velocity profiles of probe 3 showed a clear wind velocity acceleration at the top
 233 of the circular cylinder model, while the wind velocity was gradually accelerated in all the Buddha statue cases
 234 at this point as shown in Figure 7. A similar wind velocity acceleration was observed at the top of both the
 235 models in the mean along-wind velocity profile of probe 4. Therefore, the flow separation only occurred closer
 236 to the top rear head of the Buddha statue within the studied wind direction regions. In the mean across-wind
 237 velocity profiles, considerable variations were observed in-between 0.15 to $0.25 H$ and 0.7 to $1.0 H$ at probe 4
 238 for the Buddha statue $\alpha = 90^\circ$ case. Since these changes were the largest among all the simulation cases, the
 239 wake flow in these regions were mostly highly asymmetric or unsteady compared to those in the other regions.

240 Flow Field Around the Circular Cylinder

241 A horseshoe vortex was observed in front of the circular cylinder model as shown in Figure 8 (a) and
 242 (b). At the top part of this model, the flow separated at the leading edge and reattached at the trailing edge. The
 243 downwash from the top of the circular cylinder produced massive and small vortices in the upper and lower
 244 halves of the wake region, respectively. These flows agreed well with the results in existing literature (Pattenden
 245 et al., 2005). As shown in Figure 9 (a), the lower vertical vortex in the xz -plane extended from the ground to 0.2
 246 H while the upper vertical vortex extends from 0.25 to $1.0 H$. A small horseshoe vortex was observed at $0.88 B$
 247 from the front surface of the circular cylinder at $z/H = 0.006$ as shown in Figure 9 (b), indicating 3D boundary
 248 layer separation. In the wake region of the xy -plane, the two symmetric vortices, which were denoted as a paired
 249 vortex, started to appear from 0.06 to $0.37 H$ with an increasing d' of 0.75 to $0.80 B$ and L_r of 1.68 to $1.75 B$ as
 250 shown in Figure 9 (c) and (d). However, the values started to decrease after $0.37 H$ till the top was reached. Since
 251 a reduction in the wake width suggested a reduction in the time-averaged momentum loss in the wake region,
 252 smaller loadings on the model could be expected in these regions. Near the ground surface, the d_{pair} was $0.25 B$.
 253 This value increased with increasing height, reaching a maximum of $0.55 B$ at $0.37 H$. Then, this value decreased

254 with increasing height, reaching a minimum of $0.33 B$ at $0.83 H$. Therefore, these two vortices were connected
 255 as an arch vortex at the top of the wake region as described by previous studies (Pattenden et al. 2005), with the
 256 base of the arch vortex quite close to each vortex, contrary to their positions. No obvious vortex was observed
 257 behind the circular cylinder on the xy -plane after $0.83 H$ while two tip vortices were observed at $1.01 H$, as in
 258 Figure 9 (e) and (f).

259 **Flow Field Around the Buddha Statue**

260 A horseshoe vortex was observed in front of the Buddha statue in all cases, indicating 3D boundary
 261 layer separation as shown in Figure 8 (c), (d), (e) and (f). Unlike the circular cylinder, the horseshoe vortex was
 262 located further from the front surface of the model, and the smooth and round-shaped head of the Buddha statue,
 263 which functioned as a roof, smoothly passed the flow into the wake region. Therefore, flow separation occurred
 264 closer to the trailing edge of the Buddha statue. When the wind blew from 0 , 5 , and 50° AOAs, the model was
 265 bluff, resulting in a larger wake, and the slope of the downwash from the top was more moderate than that of the
 266 circular cylinder. At $\alpha = 90^\circ$, the downwash slope was steep, and the vortices in the wake region are different
 267 from that in the rest AOAs.

268 In $\alpha = 0^\circ$ case, as shown in Figure 10 (a), the lower vertical vortex in the xz -plane has centre around
 269 $0.02 H$ while the upper vertical vortex has centre around $0.72 H$. A small horseshoe vortex was observed at 1.29
 270 B from the front surface at $0.006 H$ as shown in Figure 10 (b). In the wake region of the xy -plane, the L_r value
 271 decreased from 2.40 to $0.17 B$ with the increase in the statue's height from 0.06 to $0.98 H$, as shown in Figure
 272 10 (c) and (f). On the other hand, the vortex pair started to appear from 0.06 to $0.37 H$ with an increasing d' value
 273 of 0.95 to $1.36 B$ and an increasing d_{pair} value of 0.62 to $1.09 B$ as in Figure 10 (d). However, the d_{pair} value
 274 decreased after $0.37 H$, and the upper vortex from the vortex pair dissolved at $0.71 H$ as shown is Figure 10 (e).
 275 Two small vortices were still observed near the statue at $0.75 H$ and no obvious vortex on the xy -plane was found
 276 afterwards. A small recirculation region was observed at $0.98 H$ where sudden changes in shape between the
 277 forehead and top of the statue occurred.

278 In $\alpha = 5^\circ$ case, as shown in Figure 11 (a), the lower vertical vortex in the xz -plane has centre around
 279 $0.02 H$ while the upper vertical vortex has centre around $0.70 H$. A horseshoe vortex was observed at $1.09 B$
 280 from the front surface at $0.006 H$ as shown in Figure 11 (b). However, only one vortex was observed on the

281 lower side of the xy -plane at $0.06 H$ as illustrated in Figure 11 (c). Then, an uneven pair vortex was generated at
 282 $0.10 H$ as shown in Figure 11 (d) and developed into similar vortices of $\alpha = 0^\circ$ with a similar mechanism till 0.64
 283 H . The two vortices from the uneven vortex pair combined somewhere between 0.67 and $0.71 H$. Subsequently,
 284 no obvious vortices were observed afterward.

285 In $\alpha = 50^\circ$ case, as shown in Figure 12 (a), the lower vertical vortex in the xz -plane has centre around
 286 $0.25 H$ while the upper vertical vortex has centre around $0.65 H$. At $0.006 H$, the horseshoe vortex was observed
 287 at $1.05 B$ from the front surface of the statue as shown in Figure 12 (b). Throughout the statue's overall height,
 288 the L_r value varied between 1.81 and $0.20 B$, and the d' value varied between 0.31 and $0.92 B$. The vortex
 289 generation in the $\alpha = 50^\circ$ case started from the upper side of the xy -plane at $0.06 H$, and then, a vortex pair was
 290 developed at $0.14 H$ as shown in Figure 12 (c) and (d). The vortex pair dissolved at $0.56 H$ as in Figure 12 (e)
 291 and moved towards the statue as smaller vortices between 0.60 and $0.67 H$. No obvious vortex was observed
 292 around the statue between 0.71 and $0.83 H$ while small vortices could be observed around the statue afterwards
 293 as illustrated in Figure 12 (f).

294 Since the statue was streamlined in the $\alpha = 90^\circ$ case, it had the smallest wake region in this case, and it
 295 also had more vortices. As shown in Figure 13 (a), the lower vertical vortex in the xz -plane has centre around
 296 $0.07 H$, the middle vertical vortex has centre around $0.52 H$ and the upper vertical vortex has centre around 0.95
 297 H . As illustrated in Figure 13 (b), the horseshoe vortex was observed at $0.95 B$ from the front surface of the
 298 statue at $0.006 H$. On the xy -plane, the pair vortex was generated starting from 0.10 till $0.33 H$, with the increasing
 299 L_r value of 1.24 to $1.31 B$, the decreasing d' value of 0.70 to $0.56 B$, and the d_{pair} value of 0.39 to $0.37 B$ as
 300 illustrated in Figure 13 (c) and (d). Afterward, the vortex on the lower side of the wake region (the same side as
 301 the setback of the model) became smaller. Only one upper vortex was observed at $0.52 H$ with a L_r of $1.03 B$ and
 302 d' of $0.50 B$ as shown in Figure 13 (e). While L_r and d' continued to decrease, no obvious vortex was found within
 303 0.56 – $0.67 H$. A small vortex reappeared on the upper side of the wake region at $0.71 H$ and developed into two
 304 vortices at $0.75 H$ as illustrated in Figure 13 (f). Later, this was reduced to one vortex on the lower side between
 305 0.79 and $0.83 H$. This vortex developed into a vortex pair once more between 0.86 – $0.90 H$. No obvious vortex
 306 was found at $0.94 H$ but a small vortex pair was found again in the wake region at $0.98 H$.

307 Hence, we inferred that the width of the wake region was highly influenced by the shape of the model,
308 and that the formation of vortices in the wake region was complex.

309 WIND RESISTANCE EVALUATION OF BUDDHA STATUE

310
311 Wind loading on structures is an important consideration made in structural design, as it can
312 significantly affect the safety of the structure. Furthermore, the effects of wind on structures can be divided into
313 two types: static and dynamic. In this study, the mean aerodynamic force coefficients (C_{Fx} , C_{Fy}) and Strouhal
314 number (St) for the studied cases with different AOAs were calculated to determine how the flow patterns around
315 the Buddha statue could affect its structure.

316 Aerodynamic Coefficients (C_{Fx} , C_{Fy})

317 During the LES simulation, the pressure and wind velocity acting on and around the Buddha statue were
318 recorded. The mean wind forces were calculated by integrating the pressure around the surface area of each part.
319 The mean force coefficients were calculated as follows:

$$320 \quad C_{Fi} = \frac{F_i}{\frac{1}{2}\rho U_{H_j}^2 A_j} \quad (7)$$

321 where F_i ($i = x, y$) is the mean force of each model part along the x and y directions, A_j is the frontal surface area
322 of part j , ρ is the air density, and U_{H_j} is the mean wind speed at the mid-height of part j .

323 The mean wind force coefficients of the circular cylinder and Buddha statue are shown in Figure 14.
324 The mean along-wind force coefficient (C_{Fx}) of the circular cylinder model was 1.53 at $0.02 H$ and within 0.86–
325 1.06 between 0.06 – $0.94 H$. The C_{Fx} value changed from following a decreasing trend to following an increasing
326 one around $0.33 H$ where the main upper and lower vertical vortices were reattached vertically on the xz -plane.
327 At $0.98 H$, the value of C_{Fx} decreased to 0.69, which might be related to the disappearance of the horizontal
328 vortex pair on the xy -plane. For the across-wind force coefficient (C_{Fy}), the value throughout the height was
329 approximately zero. Therefore, the flow separation was symmetrical, and the pressure distributions on both sides
330 of the circular cylinder were equal in the across-wind direction.

331 Sharp changes in both the C_{Fx} and C_{Fy} values were found around 0.14–0.25 H and 0.83–0.90 H of the
 332 Buddha statue in the studied wind directions. In the first region, the shape of the Buddha statue changed from
 333 rectangular to elliptical. In this region, the lower vertical vortex was reattached vertically on the xz -plane,
 334 accompanied by a horizontal vortex pair and a large wake region. Therefore, the value of C_{Fx} suddenly increased
 335 in this area. The second region was located around the neck of the Buddha statue. Here, the upper vertical vortex
 336 was reattached vertically on the xz -plane, whereas the horizontal vortex pair weakened on the xy -plane. The C_{Fx}
 337 value decreased steadily with the height from 1.69 to 0.70 for $\alpha = 0^\circ$, 1.70 to 0.70 for $\alpha = 5^\circ$, and 1.27 to 0.74
 338 for $\alpha = 50^\circ$ between 0.25 and 0.83 H . This decrease was attributed to the reduction in the wake region and vortex
 339 size near the top of the Buddha statue. However, the value of C_{Fx} remained constant between 0.29 and 0.52 H in
 340 the $\alpha = 90^\circ$ case. Since the elevator setback behind the statue ended at 0.56 H , the horizontal vortex pair
 341 transformed into a single vortex and the C_{Fx} value started to decrease from the stabilized condition until it reached
 342 0.87 H . The C_{Fx} value of the $\alpha = 90^\circ$ case was the smallest among the C_{Fx} values in all the cases because the
 343 wake region was the smallest. Similar sudden changes were observed in the C_{Fy} values. Symmetric time-averaged
 344 flow was observed only between 0.19 to 0.77 H in the $\alpha = 0^\circ$ case.

345 When the wind direction for the Buddha statue changed from 0° to 90° , the flow separation from the
 346 top remained the same. However, the slope of the downwash became steeper as illustrated in Fig. 8. This
 347 decreased the length of the recirculation region (L_r). The width of the Buddha statue decreased from 47.63 to
 348 43.47 m as AOA increased. Therefore, the width of the wake region (d') and distance between each vortex pair
 349 (d_{pair}) also decreased. As a result, the size of the overall 3D wake region behind the Buddha statue became
 350 narrower and the global mean along-wind force coefficient value decreased constantly from 1.35, 1.35, 1.08,
 351 and 0.80. On the other hand, the global mean across-wind force coefficient varied from 0.01, 0.14, -0.40, and
 352 0.40. Therefore, it was concluded that symmetric time-averaged flow was still observed at $\alpha = 0^\circ$ despite the
 353 complex shape of the Buddha statue.

354 **Strouhal Number (St)**

355 Previous studies have shown that a large amount of wind load is placed on tall structures owing to vortex
 356 shedding in the wake region behind them. According to Irwin (2010), the effects of vortex shedding on a tall
 357 building can be determined by comparing the fundamental frequency of vibration for the building (f_b) and vortex

358 shedding frequency from the building into the vortex street (f_v), where f_b is mainly dependent on the structural
359 system and mass distribution of the building. The Strouhal number (St) can be calculated as follows:

360
$$St = \frac{f_v U_{Hj}}{w_j} \quad (8)$$

361 where U_{Hj} is the mean wind velocity at the mid-height of part j , w_j is the width of part j in the along-wind
362 direction, and f_v is the vortex shedding frequency.

363 Figure 15 (a) shows the vortex shedding frequency (f_v) in all the measured cases. The f_v value of the
364 Buddha statue was approximately constant throughout the height for $\alpha = 0$ and 5° , and the value was
365 approximately half that of the circular cylinder. However, an increase in the f_v value was observed within 0.40–
366 0.70 H in the $\alpha = 50^\circ$ case, while the remaining heights had similar values of $\alpha = 0$ and 5° . The $\alpha = 90^\circ$ case,
367 wherein the setback was attached parallel to the inlet wind direction, had the highest f_v value. As this case had
368 the minimum d' and L_r values, the spacing between the vortices was small, and the f_v value increased.
369 Additionally, a phenomenon that occurred in the $\alpha = 50^\circ$ case also similarly occurred in this case, starting from
370 0.70 H . This may be related to the creation of asymmetric vortices due to the flow changes in the wake region.
371 Furthermore, the power of these frequencies was weak and difficult to capture.

372 The Strouhal number of the circular cylinder used in this study agreed well with the results reported by
373 Fox and West (1993). According to the static wind tunnel tests performed by Ma et al. (2017), the Strouhal
374 number of an elliptical cylinder is 0.18 for $Re = 1.24 \times 10^5$ and $\alpha = 26^\circ$. As the Strouhal number depends on the
375 width, wind speed, and vortex shedding frequency, variations in the St value were observed between each height
376 in all the cases, as shown in Figure 15 (b). The St value in all the cases decreased steadily from their starting
377 values during the interval between the ground and 0.16 H due to the influence of the 3D boundary layer
378 separation. Meanwhile, the St values in all the cases except the $\alpha = 50^\circ$ case were approximately close to each
379 other between 0.16 and 0.74 H . In the $\alpha = 50^\circ$ case, the St value became closer to the others only within 0.16–
380 0.47 H due to the exposure of setback to the inlet wind flow. Afterwards, the value increased to approximately
381 twice that in the remaining cases until the height reached 0.70 H . Later, the value decreased, similarly following
382 the trend that the values in the other cases did for the remaining height. A similar abrupt change in the St value

383 was also observed starting from $0.70 H$ in the $\alpha = 90^\circ$ case. The St value of the Buddha statue increased from
384 0.094 to 0.118 as the AOA increased between 0.16 and $0.47 H$ in all cases. Therefore, the statue might vibrate
385 at lower wind velocity when the AOA increased in this region. Furthermore, the abrupt change in the St value
386 increased with height, especially toward the top of the Buddha statue as the AOA increased. Thus, wind-induced
387 vibration responses of this structure may vary largely depending on the height and AOA.

388 MAINTENANCE, RENOVATION, AND MANAGEMENT

389
390 The 3D terrestrial laser scanning is a simple process and the conditions around the Buddha statue can
391 be inspected easily from the scanned data visualizations. These data can be combined with mapping or geological
392 data obtained from the GIS and used in building information modelling (BIM) for the maintenance, rehabilitation,
393 and management of the Buddha statue. In this study, wind load characteristics such as aerodynamic force
394 coefficients and vortex shedding frequencies were calculated based on a 3D model obtained by scanning to
395 complex-shaped. Afterward, the most vulnerable parts of the Buddha statue which might require maintenance
396 were noted based on the numerical investigation results acquired using 3D visualization data.

397 Based on the flow field analysis around the Buddha statue, it was expected to obtain higher along-wind
398 forces at $\alpha = 0$ and 5° . For all studied AOAs, the along-wind force coefficient was largest at the base and
399 decreased toward the top as shown in Figure 14. Therefore, the lower part of the statue, such as under $0.2 H$,
400 may require strengthening as time passed. Furthermore, both the C_{Fx} and C_{Fy} values indicated that sudden force
401 changes could occur within $0.14\text{--}0.25 H$ and $0.83\text{--}0.90 H$. This may have a noticeable influence on the
402 serviceability and structural safety of the Buddha statue on closer inspections. Hence, the strength of the
403 connection between the lotus throne and the feet ($0.14\text{--}0.25 H$) and neck ($0.83\text{--}0.90 H$) of the Buddha statue
404 need to be increased during its maintenance and renovation. As the statue has relatively a small mass as it is a
405 hollow structure, whether wind loading governed the lateral load design of the statue should be checked during
406 the analysis for the maintenance and renovation. Additional vertical and diagonal bracings could be added inside
407 the statue to increase wind load resistance if it is necessary. The strength of these bracings should be checked
408 and strengthened on a timely basis, to efficiently reduce the effects of wind-induced loads on the statue.

409 As the height of the statue becomes higher, the natural frequency is expected to become smaller as the
410 statue becomes slender and the setback behind the statue discontinues. On the other hand, the Kármán vortex
411 shedding frequency became higher as the AOA increased. Resonant (lock-in) wind load will arise when the
412 vortex shedding frequency is close to the natural frequency of the structure. In addition, this can induce vibrations
413 that decrease occupant comfort, reduce serviceability and lead to structural failure. If the accelerometer, impact
414 test, and modal analysis are possibly to be carried out, the natural frequency of the Buddha statue could be
415 calculated. Then, the resonant wind load on the Buddha statue can be determined based on the Kármán vortex
416 shedding frequency values provided in this study, and the proper maintenance and renovation plan for the
417 Buddha statue can be implemented for each story level. Therefore, appropriate preventative measures for
418 noticeable vibrations may be possible in the future design of a similar structure.

419 Since the across-wind response dominates wind loading at higher wind speeds and is mainly caused by
420 vortex shedding, many structures modify the shapes around their corners, cross-sections, and heights to reduce
421 the amount of wind loading and vibrations caused by vortex shedding. In the Buddha statue under study, one
422 setback was present at the back between 0.14 and $0.56 H$. After this setback, abrupt changes in the Strouhal
423 number were observed. The locations where these abrupt changes occurred moved to a higher height with the
424 increase in the AOA. Since the increase in Strouhal number means an increase in instability, aerodynamic
425 modification such as slotted corners, baffles, and fins should be considered when renovating to reduce the
426 instability of the Buddha statue.

427 The horseshoe vortex, which was observed upstream, moved closer to the Buddha statue with an
428 increased AOA, as listed in Table 1. Hence, the construction materials between the ground surface and $0.10 H$
429 should be strengthened periodically to withstand material deterioration and avoid collapse during high winds
430 such as tropical cyclones. The Buddha statue has a large wake with L_r of $2.64B$ and d' of $1.36B$. This may
431 significantly affect the wind flow field and wind load acting on the surrounding structures. This should also need
432 to consider in the structural management of the surrounding structures.

433 CONCLUSIONS

434

435 In this study, the wind resistance of an existing complex-shaped standing Buddha statue was evaluated
436 using 3D terrestrial laser scanning and Large Eddy Simulation (LES). Flow visualization was performed to
437 obtain a full picture of the flow around the statue and to investigate the flow structures in the separation regions
438 for different shapes of the statue. Based on the results, the following conclusions were drawn regarding 3D laser
439 scanning; and the flow field characteristics, aerodynamic characteristics, and management of the Buddha statue.

440 (1) As black surfaces have less reflectivity and cannot return sufficient laser pulses to create a point
441 cloud, the scanner could not collect complete data on the black hair of the Buddha statue. These imperfections
442 can be treated with third-party software. The 3D terrestrial laser scanning method was easy to operate and could
443 reproduce fairly precise 3D models of massive, tall, and complex-shaped structures within a short period of time.

444 (2) Owing to the variations in the surface, cross-sectional shape, and the presence of setbacks throughout
445 the height of the Buddha statue, the flow field around the statue contained many small vortices, and the 3D arch
446 vortex in the wake region intertwined in a complex manner. The time-averaged flow fields in the xz -plane and
447 different xy -planes of the studied cases with different angle of attacks (AOA) showed that the wake region size
448 decreased and the horseshoe vortex moved closer toward the Buddha statue as the AOA increased. Furthermore,
449 the size of the wake region depended not only on the width of the model, but also on the flow separation
450 conditions. Tip vortices were not observed at the top of the Buddha statue, whereas a small recirculation zone
451 was observed on the windward side at the top. Therefore, the vortex shedding near the top was different from
452 that at the remaining height, and the interaction between the flow and leading edge was very small at the top of
453 the Buddha statue. The Strouhal number of the Buddha statue increased and the abrupt changes in the value
454 moved towards the top of the Buddha statue as the AOA increased. Hence, this structure is likely to be affected
455 by flow-induced vibrations when the AOA changed and this also needs to be considered in the structural design
456 and maintenance.

457 (3) The Buddha statue behaved as a bluff body when the AOAs were 0, 5, and 50°, whereas it behaved
458 as a streamlined body at 90°. Accordingly, the $\alpha = 90^\circ$ case had the smallest wake region size and minimum
459 along-wind force coefficient among the studied cases. Based on the across-wind force coefficient, the symmetric
460 time-averaged flow was only observed within 0.19–0.77 H under the $\alpha = 0^\circ$ case. The presence of a setback on
461 the back of the Buddha statue increased the Strouhal number after 0.50 H for cases with higher AOAs. This

462 abrupt increase moved towards a higher height as the AOA increased. Furthermore, the horseshoe vortex with
463 $0.10 H$ moved closer toward the Buddha statue as the AOA increased. Therefore, these places should be regularly
464 inspected for maintaining the safety of the Buddha statue and protecting it against natural and man-made
465 disasters.

466 Laser scanning the Buddha statue, which was surrounded by mountainous terrains and a dam; and
467 meshing and simulating the complex-shaped Buddha statue with the setback on its back were some of the
468 challenges encountered during this study. To address these large challenges, various unconventional methods
469 were required. With the higher demand for economical and time-efficient methods for accurate wind response
470 evaluation, the methods highlighted in the previous sections can be considered in evaluating tall complex-shaped
471 structures where field testing is difficult or infeasible. In the future, more research on long-term structural health
472 monitoring, life-cycle performance evaluation, and the risk analysis of unique structures should be conducted. It
473 is also an alternative to apply power law and consider topographic effects in the future simulation.

474 **DATA AVAILABILITY STATEMENT**

475 All data, models, or codes that support the findings of this study are available from the corresponding author
476 upon reasonable request.

477 **ACKNOWLEDGEMENTS**

478 We would like to express our heartfelt gratitude to the late Professor, Dr. Hiromichi Shirato, Department
479 of Civil and Earth Resources Engineering, Kyoto University, for the indispensable guidance and advice. We also
480 express our deep gratitude to the late president of the Myanmar Engineering Society (Monywa), Engr. Aung
481 Kyaw Myint, for help during 3D laser-scanning. We are grateful to the Assistant Director, Dr. Kyaw Zaya Htun,
482 Remote Sensing, and GIS Research Center, Yangon Technological University (YTU); Engr. Thant Zin Win; and
483 the students from YTU for their interest and help during the laser-scanning trip. The supercomputer of ACCMS,
484 Kyoto University, was used for flow simulation.

485 **DECLARATION OF INTEREST STATEMENT**

486 The authors report there are no competing interests to declare.

487 **REFERENCES**

- 488 AIJ (Architectural Institute of Japan). 2017. Guidebook of Recommendations for Loads on Buildings 2. Wind-
489 induced Response and Load Estimation/Practical Guide of CFD for Wind Resistant Design, Architectural
490 Institute of Japan, (in Japanese).
- 491 Baker, W. F., D. S. Korista, and L. C. Novak. 2007. “Burj Dubai: Engineering the world’s tallest building.”
492 *Structural Design of Tall and Special Buildings*, 16 (4). <https://doi.org/10.1002/tal.418>.
- 493 Dagnew, A. K., and G. T. Bitsuamlak. 2013. “Computational evaluation of wind loads on buildings: A review.”
494 *Wind and Structures, An International Journal*.
- 495 Fox, T. A., and G. S. West. 1993. “Fluid-Induced loading of cantilevered circular cylinders in a low-turbulence
496 uniform flow. Part 1: Mean loading with aspect ratios in the range 4 to 30.” *Journal of Fluids and Structures*,
497 7 (1). <https://doi.org/10.1006/jfls.1993.1001>.
- 498 Hess, M., V. Petrovic, M. Yeager, and F. Kuester. 2018. “Terrestrial laser scanning for the comprehensive
499 structural health assessment of the Baptistery di San Giovanni in Florence, Italy: an integrative
500 methodology for repeatable data acquisition, visualization and analysis.” *Structure and Infrastructure*
501 *Engineering*, 14 (2). <https://doi.org/10.1080/15732479.2017.1349810>.
- 502 Hirano, A. 2021. “Effects of climate change on spatiotemporal patterns of tropical cyclone tracks and their
503 implications for coastal agriculture in Myanmar.” *Paddy and Water Environment*, 19 (2).
504 <https://doi.org/10.1007/s10333-021-00842-x>.
- 505 Irwin, P. A. 2010. “Vortices and tall buildings: A recipe for resonance.” *Physics Today*, 63 (9).
506 <https://doi.org/10.1063/1.3490510>.
- 507 Irwin, P., J. Kilpatrick, J. Robinson, and A. Frisque. 2008. “Wind and tall buildings: Negatives and positives.”
508 *Structural Design of Tall and Special Buildings*.
- 509 Ma, W., J. H. G. Macdonald, and Q. Liu. 2017. “Aerodynamic characteristics and excitation mechanisms of the
510 galloping of an elliptical cylinder in the critical Reynolds number range.” *Journal of Wind Engineering*
511 *and Industrial Aerodynamics*, 171. <https://doi.org/10.1016/j.jweia.2017.10.006>.
- 512 Mavriplis, D. J. 2007. “Unstructured mesh discretizations and solvers for computational aerodynamics.”
513 *Collection of Technical Papers - 18th AIAA Computational Fluid Dynamics Conference*.

- 514 Mavriplis, D. J. 2008. “Unstructured-mesh discretizations and solvers for computational aerodynamics.” *AIAA*
515 *Journal*.
- 516 MNBC (Myanmar National Building Code). 2016. Part 3: Structural Design, Myanmar National Building Code,
517 Second Edition.
- 518 OpenFOAM. 2019. OpenFOAM v6 User Guide: 4.4 Numerical Schemes, Retrieved from
519 <https://cfdirect.openfoam/user-guide/v6-fvschemes/>.
- 520 Pattenden, R. J., S. R. Turnock, and X. Zhang. 2005. “Measurements of the flow over a low-aspect-ratio cylinder
521 mounted on a ground plane.” *Experiments in Fluids*, 39 (1). <https://doi.org/10.1007/s00348-005-0949-9>.
- 522 van Phuc, P., T. Nozu, H. Kikuchi, K. Hibi, and Y. Tamura. 2018. “Wind pressure distributions on buildings
523 using the Coherent structure smagorinsky model for LES.” *Computation*, 6 (2).
524 <https://doi.org/10.3390/COMPUTATION6020032>.
- 525 Roshko. 1954. “On the drag and shedding frequency of two-dimensional bluff bodies.” *NACA Technical Note*
526 *3169*, (July 1954).
- 527 Smagorinsky, J. 1963. “General circulation experiments with the primitive equations I. The basic experiment.”
528 *Monthly Weather Review*, 91 (3).
- 529 Smits, A. J., and Lim, T. T. (2000). *Flow Visualization: Techniques and Examples*, Imperial College Press, First
530 edition.
- 531 Spalding, D. B. 1960. “A single formula for the ‘law of the wall.’” *Journal of Applied Mechanics, Transactions*
532 *ASME*, 28 (3). <https://doi.org/10.1115/1.3641728>.
- 533 UNDP (United Nations Development Programme). 2011. *Multi Hazard Risk Assessment in Rakhine State of*
534 *Myanmar*, Final Report, December.
- 535 Yoon, D. H., K. S. Yang, and C. B. Choi. 2010. “Flow past a square cylinder with an angle of incidence.” *Physics*
536 *of Fluids*, 22 (4). <https://doi.org/10.1063/1.3388857>.

537 **TABLES**

538

539 **Table 1.** Location of horseshoe vortex

Angle of attack, α ($^{\circ}$)	Distance from the front surface of the Buddha statue (B)
0	1.29
5	1.09
50	1.05
90	0.95

540 **LIST OF FIGURE CAPTIONS**

- 541
- 542 **Fig. 1.** Sketch of the time-averaged flow around the finite circular cylinder (Not in scale).
- 543 **Fig. 2.** Laykyun Sekkya Standing Buddha Statue.
- 544 **Fig. 3.** (a) Scanner locations (Maps Data: Google, ©2018 CNES/ Airbus, DigitalGlobe) (b) Draft scan at the
545 base viewpoint.
- 546 **Fig. 4.** (a) Unregistered scan (b) Targets at two different scans (c) Project point clouds.
- 547 **Fig. 5.** 3D model of the Buddha statue.
- 548 **Fig. 6.** (a) Computational domain dimension (Not in scale) (b) Locations of the probe (c) Mesh around the
549 Buddha statue and (d) Mesh around the circular cylinder
- 550 **Fig. 7.** Mean velocity profiles in the wake region at probes 3, 4, 9, and 10.
- 551 **Fig. 8.** 3D mean velocity streamlines around circular cylinder: (a) side view (b) top view; and around Buddha
552 statue: (c) side view at $\alpha = 5^{\circ}$ (d) side view at $\alpha = 50^{\circ}$ (e) side view and (f) top view at $\alpha = 90^{\circ}$.
- 553 **Fig. 9.** Time-averaged flow field around the circular cylinder on (a) xz-plane at $y/B=0$ and xy-plane at (b) 0.006,
554 (c) 0.06, (d) 0.37, (e) 0.83, and (f) 1.01 H.
- 555 **Fig. 10.** Time-averaged flow field around the Buddha statue at $\alpha = 0^{\circ}$ on (a) xz-plane at $y/B=0$ and xy-plane at
556 (b) 0.006, (c) 0.06, (d) 0.37, (e) 0.71, and (f) 0.98 H.
- 557 **Fig. 11.** Time-averaged flow field around the Buddha statue at $\alpha = 5^{\circ}$ on (a) xz-plane at $y/B=0$ and xy-plane at
558 (b) 0.006, (c) 0.06, and (d) 0.10 H.
- 559 **Fig. 12.** Time-averaged flow field around the Buddha statue at $\alpha = 50^{\circ}$ on (a) xz-plane at $y/B=0$ and xy-plane at
560 (b) 0.006, (c) 0.06, (d) 0.14, (e) 0.56, and (f) 0.98 H.

561 **Fig. 13.** Time-averaged flow field around the Buddha statue at $\alpha = 90^\circ$ on (a) xz-plane at $y/B=0$ and xy-plane at
562 (b) 0.006, (c) 0.10, (d) 0.33, (e) 0.52, and (f) 0.75 H.

563 **Fig. 14.** Mean wind force coefficients.

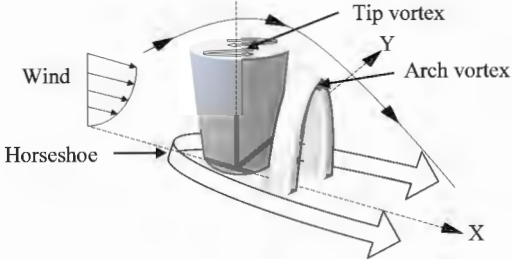
564 **Fig. 15.** (a) Vortex shedding frequency in the wake region (b) Strouhal number



京都大学
KYOTO UNIVERSITY

A Self-Archived copy in

京都大学学術情報リポジトリ
Kyoto University Research Information Repository
KURENAI
kyoto-u.ac.jp





京都大学
KYOTO UNIVERSITY

京都大学学術情報リポジトリ
Kyoto University Research Information Repository
KURENAI
京都大学学術情報リポジトリ
Kyoto University Research Information Repository

紅



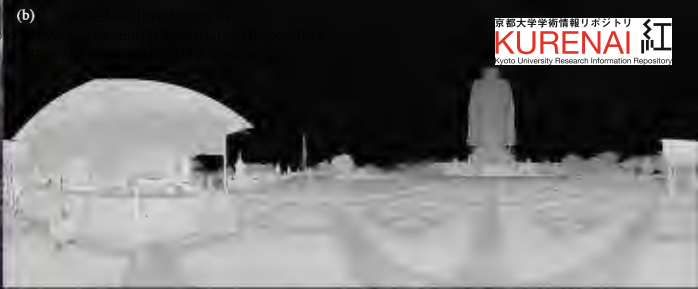
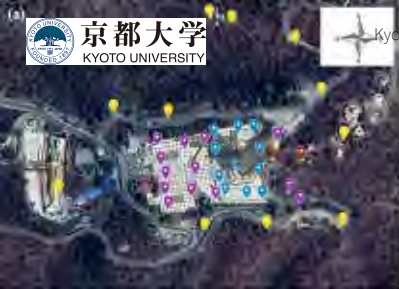


京都大学
KYOTO UNIVERSITY



(b)

京都大学学術情報リポジトリ
KURENAI
Kyoto University Research Information Repository





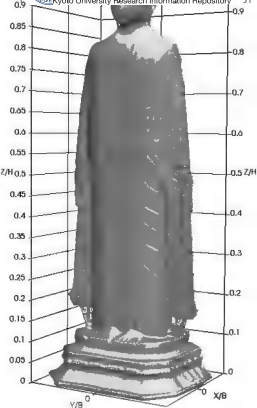
京都大学
KYOTO UNIVERSITY

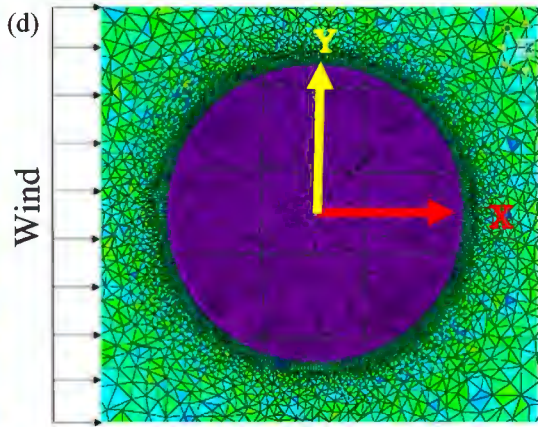
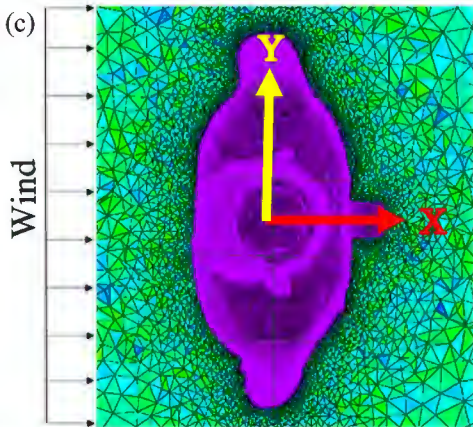
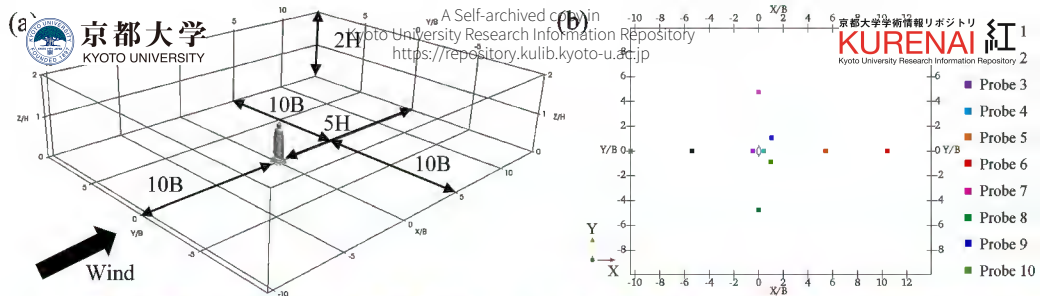
(b) Self-archived copy in
Kyoto University Research Information Repository
<https://repository.kulib.kyoto-u.ac.jp>

(c)

京都大学学術情報リポジトリ
KURENAI 紅
Kyoto University Research Information Repository









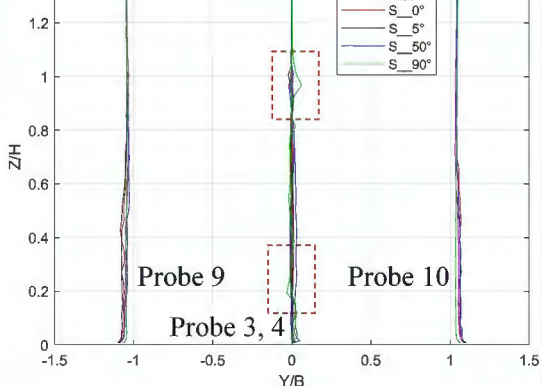
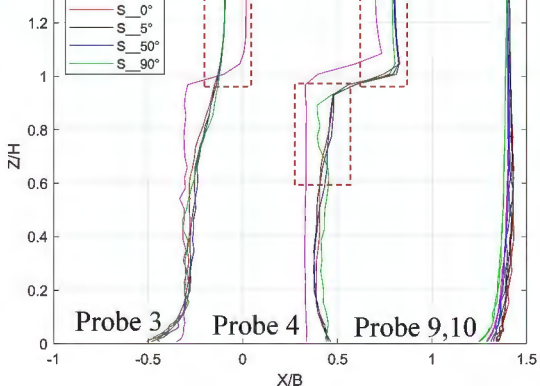
京都大学
KYOTO UNIVERSITY

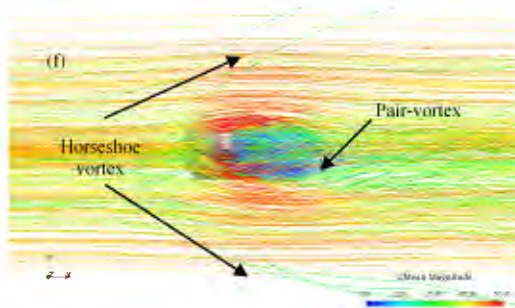
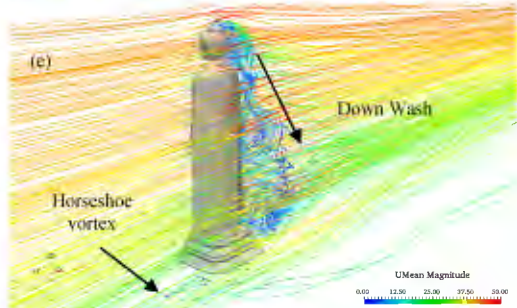
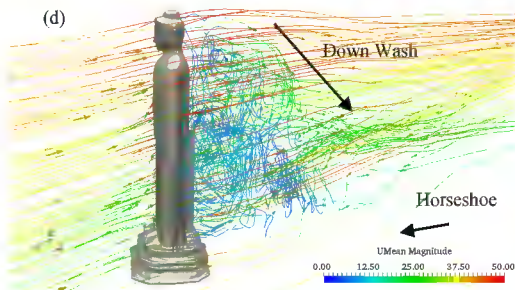
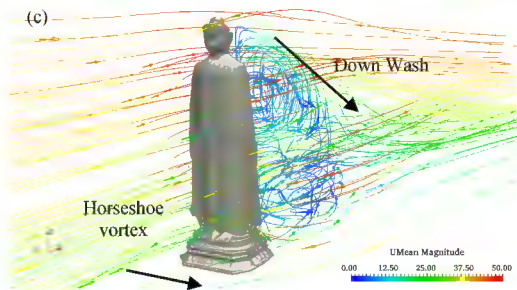
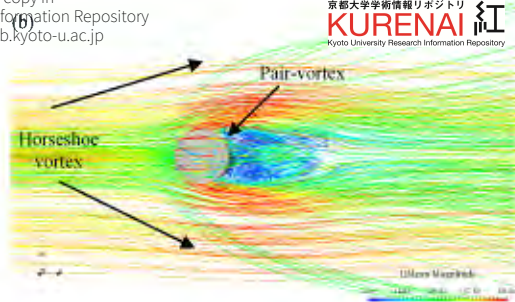
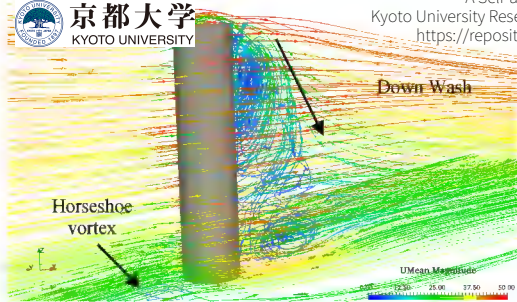
AlongWind Profile (2D)

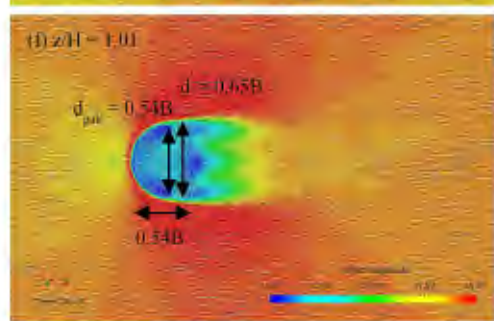
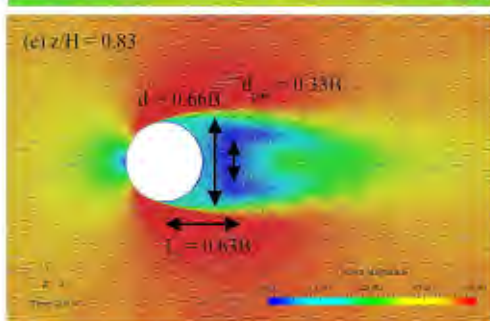
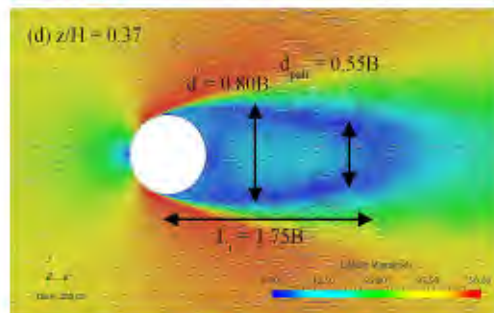
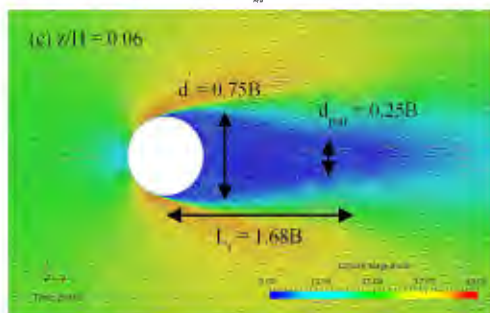
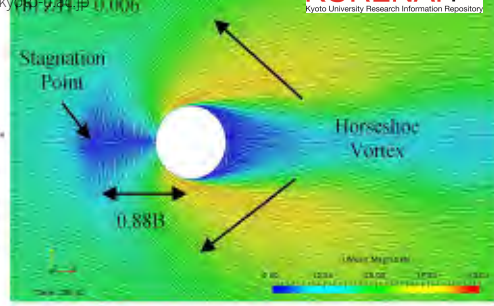
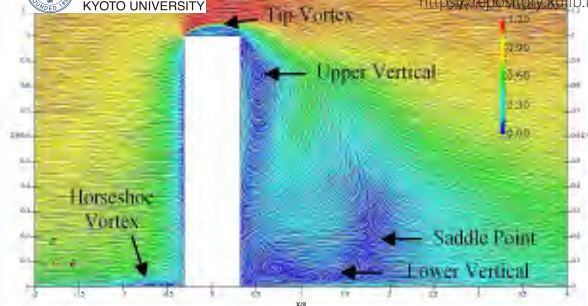
A Self-archived copy in
Kyoto University Research Information Repository
<https://repository.kulib.kyoto-u.ac.jp>

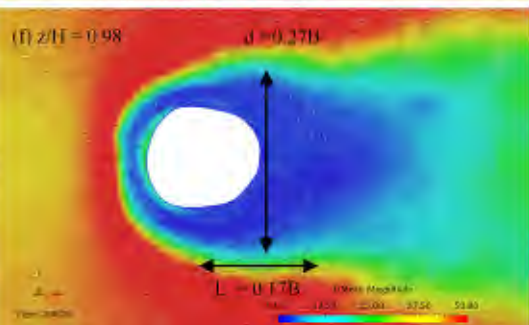
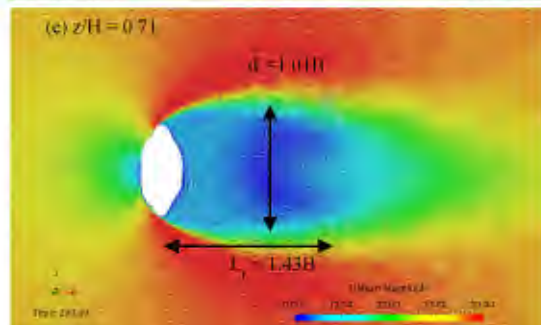
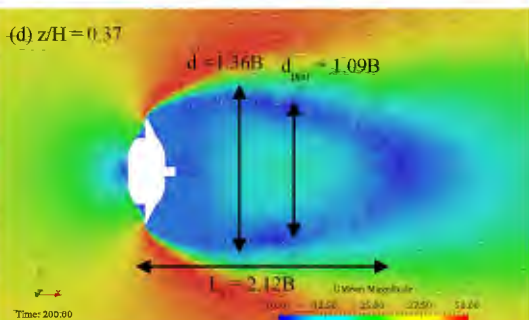
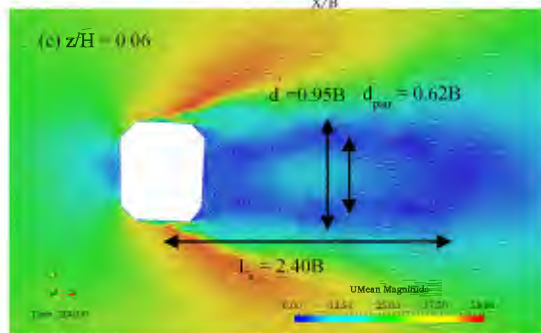
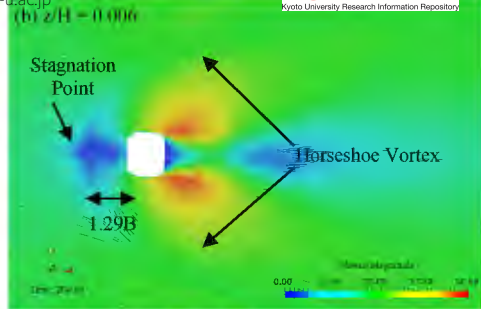
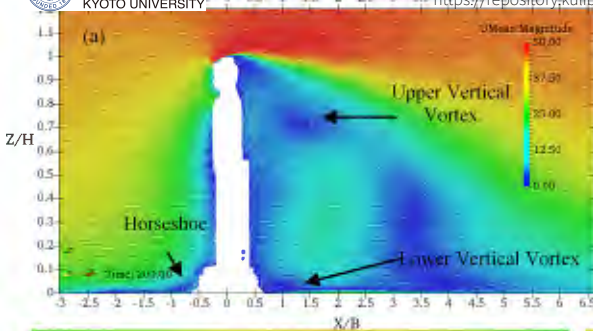
CrossWind Profile

京都大学学術情報リポジトリ
KURENAI
Kyoto University Research Information Repository



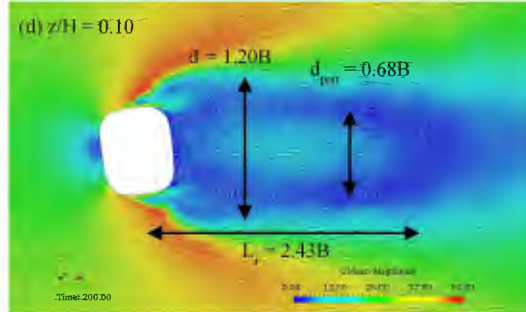
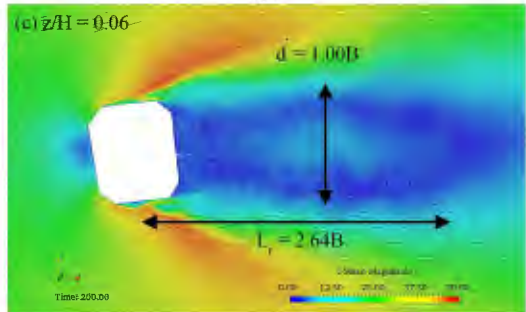
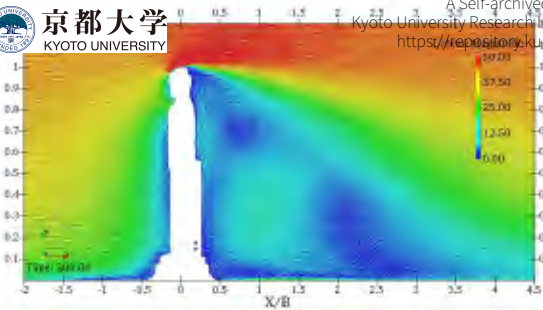


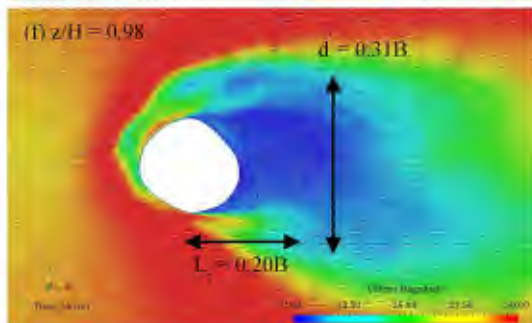
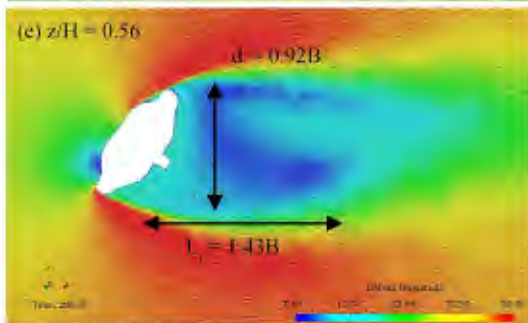
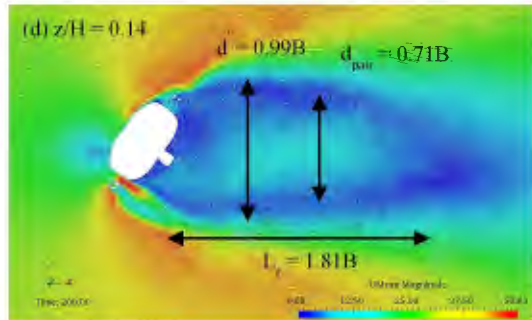
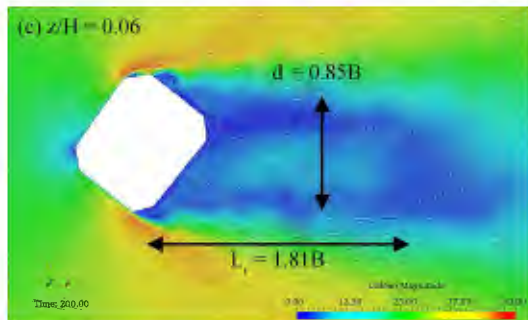
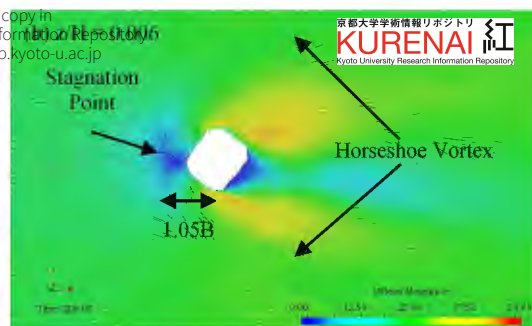
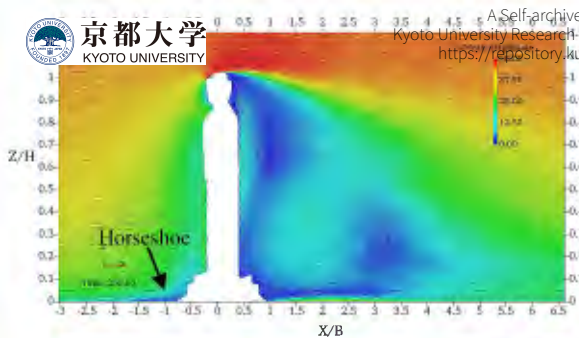


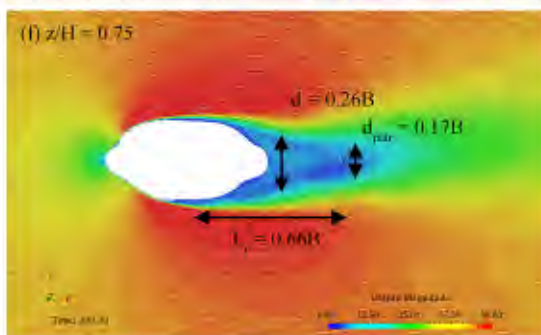
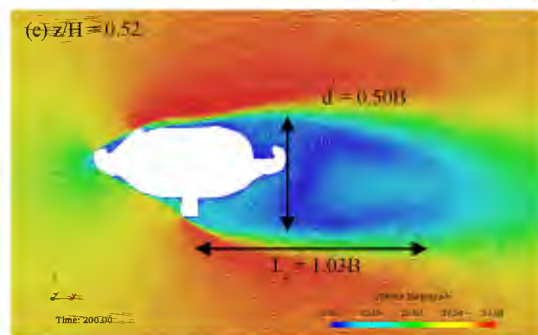
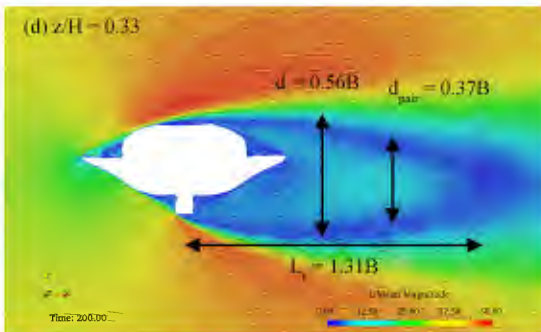
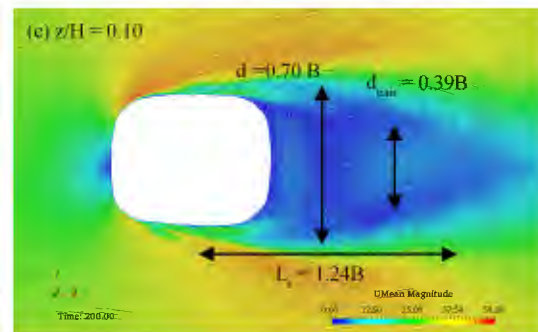
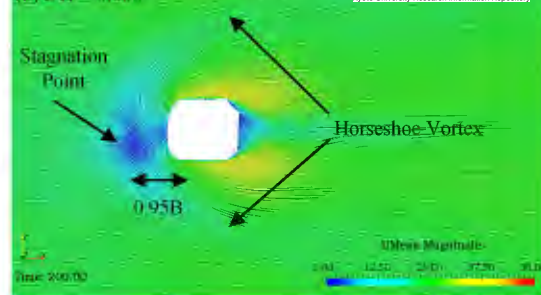
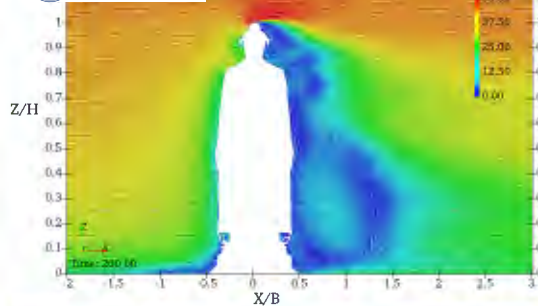




Z/H



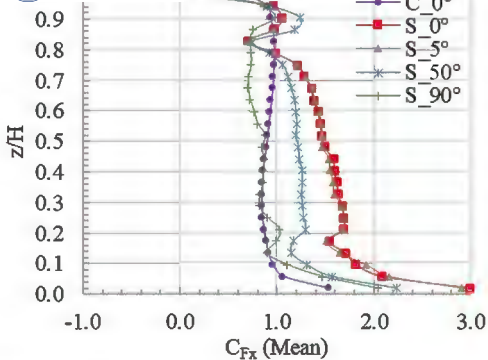






京都大学

KYOTO UNIVERSITY

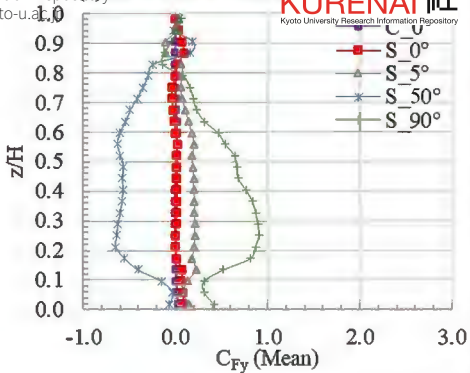


A Self-archived copy in

Kyoto University Research Information Repository

<https://repository.kulib.kyoto-u.ac.jp/>

(b) Mean cross-wind coefficient (C_{Fy})



京都大学学術情報リポジトリ
KURENAI
Kyoto University Research Information Repository

